



A promising strontium and cobalt-free $\text{Ba}_{1-x}\text{Ca}_x\text{FeO}_{3-\delta}$ air electrode for reversible protonic ceramic cells

Guangjun Zhang^a, Ting Chen^{a,*}, Yuechao Yao^b, Chenxiao Wang^a, Xiaonan Bao^a,
Guozhu Zheng^a, Zuzhi Huang^c, Xiaoyu Zhang^a, Kui Liu^a, Lang Xu^a, Yucun Zhou^{b,*},
Shaorong Wang^{a,*}

^a School of Chemistry and Chemical Engineering, China University of Mining and Technology, 1 Daxue Street, Xuzhou, Jiangsu Province 221116, China

^b Beijing Huairou Laboratory, Beijing 101400, China

^c Jiangxi Key Laboratory of Surface Engineering, School of Materials and Energy, Jiangxi Science and Technology Normal University, Nanchang, Jiangxi Province 330013, China

ARTICLE INFO

Keywords:

Reversible protonic ceramic cells

Strontium and cobalt-free

$\text{Ba}_{1-x}\text{Ca}_x\text{FeO}_{3-\delta}$

Triple conduction

ABSTRACT

The air electrode with strontium and cobalt elements has the elemental diffusion or delamination issue on the air electrode/electrolyte interface in reversible protonic ceramic cells (RPCCs). Hence the development of strontium and cobalt-free triple conducting ($\text{H}^+/\text{O}^{2-}/\text{e}^-$) air electrodes with high electrochemical activity and stability is urgent. Here, we report a strontium and cobalt-free $\text{Ba}_{0.8}\text{Ca}_{0.2}\text{FeO}_{3-\delta}$ (BCF82) air electrode with high catalytic activity and electrochemical stability for oxygen reduction/evolution reactions. A RPCC with the BCF82 air electrode shows a high peak power density of 1.14 W cm^{-2} in the fuel cell mode and a current density of 3.49 A cm^{-2} under 1.3 V in the electrolysis mode at 700°C . Furthermore, the cell demonstrates suitable stability in the fuel cell, electrolysis and reversible modes at 600°C for hundreds of hours without elemental segregation and delamination issue. This work offers an efficient approach to develop low-cost and durable air electrodes for RPCCs.

1. Introduction

Low-carbon energy technologies have been widely developed worldwide to cope with global climate change and reduce carbon emissions [1,2]. Wind and solar energy generation technologies are rising rapidly because of the characteristics of clean, efficient and zero-carbon [3]. However, the intermittency and unpredictability can lead to fluctuations in power output, which have an impact on regular operations and the deterioration of grid power quality [4,5]. Reversible protonic ceramic cells (RPCCs), which are promising for large-scale energy storage and conversion have attracted considerable attention due to their advantages in terms of low emission, high efficiency, and low cost [6,7]. As shown in Fig. 1, in the fuel cell (FC) mode, it is named as protonic ceramic fuel cells (PCFCs), which can efficiently convert the chemical energy of fuels (e.g., hydrogen and hydrocarbon) into electricity. In the electrolysis cell (EC) mode, it can be called as protonic ceramic electrolysis cells (PCECs), which can efficiently electrolyze H_2O into hydrogen using renewable energies. RPCCs are proton conducting

electrolyte-based cells with H_2O supplied or generated on the air electrode side. Despite the higher conductivity of proton-conducting electrolytes than the oxide ion-conducting counterparts, the performance of RPCCs is largely limited by the sluggish oxygen reduction/evolution reaction (ORR/OER) process at reduced temperature. It is critical to develop air electrodes with high electrocatalytic activity towards ORR/OER [8,9].

At present, the research of air electrode materials for RPCCs is mainly concentrated on the perovskite materials due to the high activity and ion/electronic conductivity [10]. $\text{La}_{0.6}\text{Sr}_{0.4}\text{Co}_{0.2}\text{Fe}_{0.8}\text{O}_{3-\delta}$ (LSCF) [11] and $\text{Ba}_{0.5}\text{Sr}_{0.5}\text{Co}_{0.8}\text{Fe}_{0.2}\text{O}_{3-\delta}$ (BSCF) [12] are the most extensively investigated air electrode materials for RPCCs, which contain strontium (Sr) and cobalt (Co). However, Sr-containing materials tend to experience strontium segregation, which can react with Zr or other elements in the electrolyte, resulting in the formation of insulating layers at the interface between the electrolyte and the air electrode [13,14]. In addition, Co-containing materials suffer from insufficient thermal mechanical stability due to the high coefficient of thermal expansion,

* Corresponding authors.

E-mail addresses: chenting@cumt.edu.cn (T. Chen), zhouyucun@hrl.ac.cn (Y. Zhou), srwang@cumt.edu.cn (S. Wang).

<https://doi.org/10.1016/j.apcatb.2024.124176>

Received 7 January 2024; Received in revised form 13 March 2024; Accepted 7 May 2024

Available online 10 May 2024

0926-3373/© 2024 Elsevier B.V. All rights are reserved, including those for text and data mining, AI training, and similar technologies.

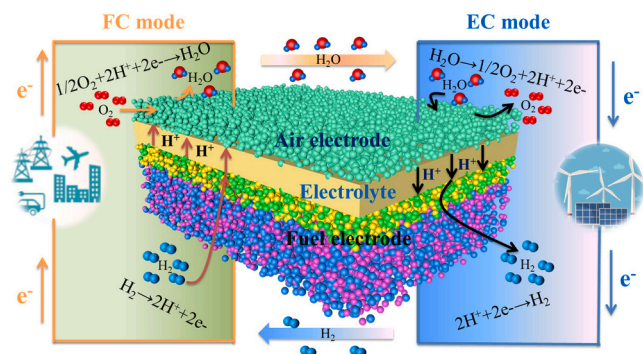


Fig. 1. Schematic illustration of reversible protonic ceramic cells.

which may cause the delamination of air electrode under cell operation conditions. Although the emerging triple conducting ($O^{2-}/H^+/e^-$) perovskite materials such as $PrBa_{0.5}Sr_{0.5}Co_{1.5}Fe_{0.5}O_{5+\delta}$ (PBSCF) [15] and $NdBa_{0.5}Sr_{0.5}Co_{1.5}Fe_{0.5}O_{5+\delta}$ (NBSCF) [16] have exhibited great potential as air electrodes for RPCCs due to the high electrochemical performance, these materials still suffer from the strontium segregation issue, especially under high concentration steam [17]. More recently, strontium-free perovskite materials with triple conduction have been reported as promising air electrodes for RPCCs, showing excellent ORR

activity and stability, such as $BaCo_{0.4}Fe_{0.4}Zr_{0.1}Y_{0.1}O_{3-\delta}$ (BCFZY) and $Ba(Co_{0.4}Fe_{0.4}Zr_{0.1}Y_{0.1})_{0.95}Mg_{0.05}O_{3-\delta}$ (BCFZYM) [18]. However, the presence of Co in the air electrode material for RPCCs still exist the risk of electrode delamination issue during the long-term operation. Therefore, it is of great significance to explore novel Sr and Co-free air electrode materials to promote the performance and long-term stability of RPCCs.

For the Ba-based perovskite oxides, for example, $BaFeO_{3-\delta}$, the large Ba ion in the A site can expand the lattice volume for the fast migration of oxygen ion. While the variable valence state element (such as Fe and Co) in the B site can promote the ORR/OER electrocatalytic activity [19, 20], the A-site doping of the $BaFeO_{3-\delta}$ with smaller alkaline-earth elements can effectively enhance the stability [21,22]. Meanwhile, the protonation of the air electrode plays a critical role in developing high-performance proton ceramic fuel cells (PCFCs), which could be promoted by doping basic elements [23]. For example, a Ca-doped $LaMnO_3$ ($La_{0.5}Ca_{0.5}MnO_{3-\delta}$) air electrode showed high performance and excellent stability for PCFCs [23]. In addition, the Ca-doping of Pr_2NiO_4 could enhance the generation of interstitial oxygen and decrease the distance between O atoms in the lattice compared with the Sr and Ba-doped Pr_2NiO_4 , thus facilitating the movement of charge carriers and enhance the catalytic activity [24].

In addition, the incorporation of Ca^{2+} ion into the A site has been demonstrated to be an effective strategy in enhancing the activity and stability of the perovskite oxides [25,26]. Furthermore, the A site doping

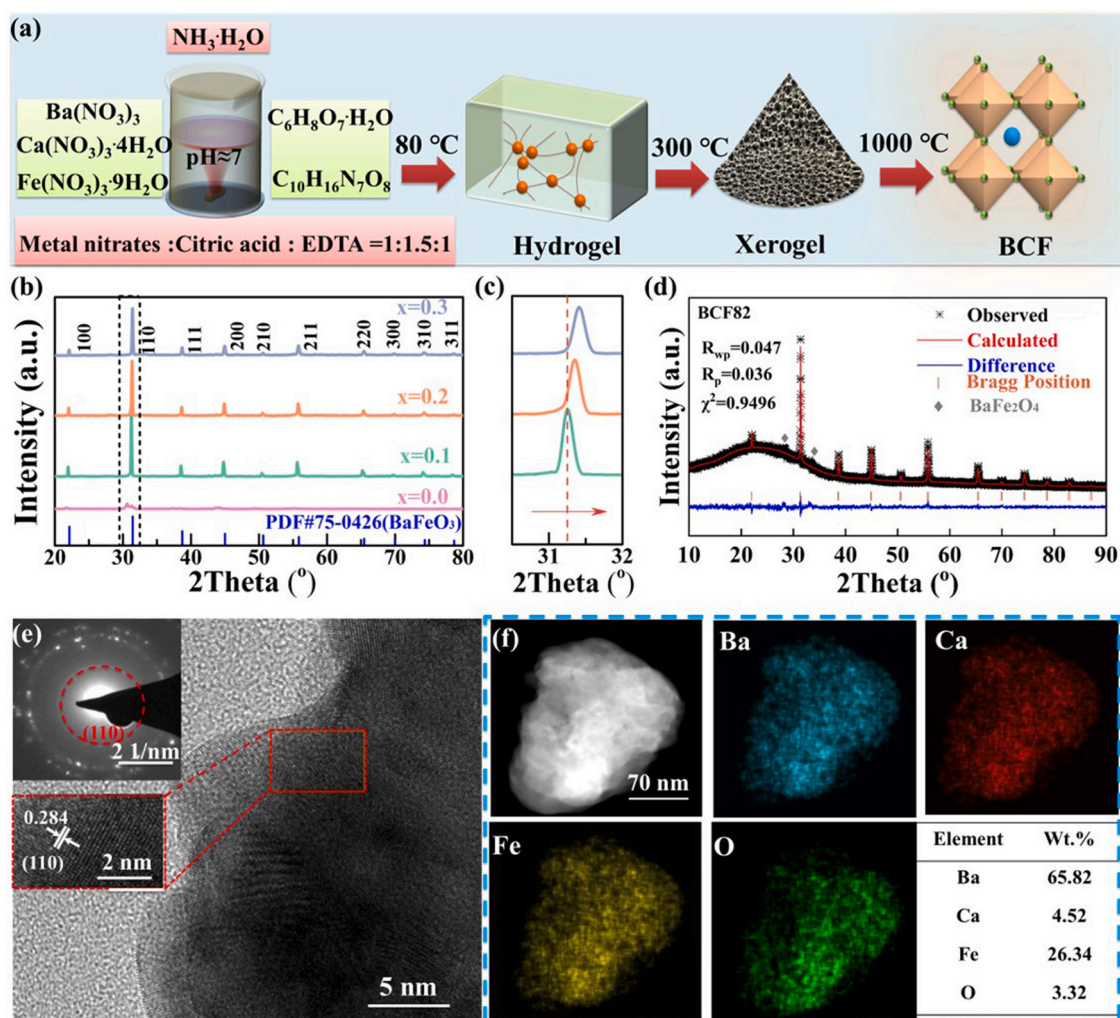


Fig. 2. Structural characterizations of $Ba_{1-x}Ca_xFeO_{3-x}$ ($x = 0, 0.1, 0.2$, and 0.3 , BCF) oxides. (a) Schematic diagram of the powder synthesis process; (b) XRD patterns of BCF with $2\theta = 20-80^\circ$; (c) Magnified view of the (110) peak of BCF in the 2θ range of $30.5-32^\circ$; (d) Refined XRD profile of the BCF82 oxide; (e) High-resolution TEM images of BCF82 grains and SAED patterns; (f) HAADF STEM image and the X-ray EDS mapping of Ba, Ca, Fe and O.

of Ca can improve the water-uptake capacity and proton conductivity of the materials, benefiting the application as air electrodes for RPCCs [27]. In this work, a series of air electrode materials were synthesized and optimized by doping Ca into the A site of $\text{BaFeO}_{3-\delta}$. The developed $\text{Ba}_{0.8}\text{Ca}_{0.2}\text{FeO}_{3-\delta}$ (BCF82) air electrode demonstrated high oxygen ion and proton conductivities, together with high ORR and OER activities. RPCCs with the BCF82 showed favorable performance and stability in both the fuel cell and electrolysis modes.

2. Fabrication, characterization, and DFT calculations

2.1. Materials synthesis

The ethylenediamine tetraacetic acid ($\text{C}_{10}\text{H}_{16}\text{N}_7\text{O}_8$, EDTA)-citrate complexing sol-gel method was utilized to synthesize the $\text{Ba}_{1-x}\text{Ca}_x\text{FeO}_{3-\delta}$ (BCF, $x=0.1, 0.2$, and 0.3) oxides. And the chemicals are all purchased from Sinopharm Chemical Reagent Co., Ltd, China. The synthesis process is shown in Fig. 2a and the details are described as follow: Firstly, $\text{Ba}(\text{NO}_3)_2$, $\text{Ca}(\text{NO}_3)_2 \cdot 4\text{H}_2\text{O}$, and $\text{Fe}(\text{NO}_3)_3 \cdot 9\text{H}_2\text{O}$ were weighed by stoichiometric ratio and dissolved in deionized water, and then EDTA, citric acid monohydrate ($\text{C}_6\text{H}_8\text{O}_7 \cdot \text{H}_2\text{O}$, CA), and ammonia hydroxide ($\text{NH}_3 \cdot \text{H}_2\text{O}$) (the molar ratio of metal ion, EDTA, and CA was 1:1.5:1) were added into the solution with a pH value of 7. The hydrogel was formed after evaporating water at 80°C and the xerogel was achieved by the followed drying at 300°C . The primary powder was grounded using mortar and pestle and then pressed into pellets with a diameter of 20 mm for further calcination. Finally, the powder was calcined at 1000°C for 5 h to yield a series of $\text{Ba}_{1-x}\text{Ca}_x\text{FeO}_{3-\delta}$ powders. The targeted air electrode paste was prepared by mixing BCF powders with a binder (5 wt% ethylcellulose dissolved in terpineol) in a mass ratio of 1:1 and ball milling for 24 h. Meanwhile, dense BCF bars prepared by the dry-pressing and sintering process (1200°C , 4 h) were used for the characterizations of conductivity and thermal expansion coefficients (TECs).

2.2. Symmetrical cells and single cells fabrication

Symmetrical cells with the configuration of BCF | $\text{BaZr}_{0.1}\text{Ce}_{0.7}\text{Y}_{0.1}\text{Yb}_{0.1}\text{O}_{3-\delta}$ (BZCYYb) | BCF were obtained by dry-pressing, screen printing, and sintering. Firstly, BZCYYb powder (Primary powder, Ruier Powder Materials Corporation, China) and 2 wt% polyvinyl butyral (PVB) were grinded in an agate mortar with alcohol solvent. The dried mixture was pressed into pellets with the diameter of 20 mm and then sintered at 1450°C for 5 h in air to achieve dense electrolytes. The BCF paste was then screen-printed on both sides of the BZCYYb electrolyte pellets, followed by sintering at 1050°C for 3 h in air. In addition, symmetrical cells with the configuration of $\text{La}_{0.6}\text{Sr}_{0.4}\text{Co}_{0.8}\text{Fe}_{0.2}\text{O}_{3-\delta}$ (LSCF, Terio Corporation, China) | BZCYYb | LSCF were prepared in the same way.

Fuel electrode supported half cells with the configuration of NiO-BZCYYb supporting layer | NiO-BZCYYb functional layer | dense BZCYYb electrolyte layer was fabricated by tape casting, hot-pressing lamination, and co-sintering as described in our previous work [28]. After that, the half cells were cut into button cells with a diameter of 15 mm. Afterward, the BCF paste was screen-printed on the BZCYYb electrolyte and sintered at 1050°C in air for 3 h. Active areas of both the symmetrical and single cells are 0.20 cm^2 . Ag-Pd paste was coated on the electrode surface as the current collector.

2.3. Characterizations and electrochemical performance tests

The phase structure of BCF powders was characterized by X-ray diffraction (XRD, Bruker D8 Advance, Germany). And the XRD refinement data were measured by step scanning method with 2° min^{-1} from 10 to 90° using $\text{Cu-K}\alpha$ radiation. High-resolution transmission electron microscope (HRTEM, FEI talos F200x G2, America) was performed to

verify the lattice parameter, crystal structure, composition, high-angle annular darkfield (HAADF) scanning transmission electron microscopy (STEM) images, and element distribution of BCF. The thermal expansion coefficients (TECs) of dense sticks were measured using the dilatometer (DIL 402 C, NETZSCH, Germany). Morphology of the cells after the stability test was observed by field emission scanning electron microscopy (FSEM, TESCAN MAIA3 LMH, Czech). Elemental distribution of the cells was measured by energy dispersive spectrum (EDS). Thermogravimetric relaxation (TGA, model STA 2500, NETZSCH) was performed to characterize the hydration reaction of BCF82. X-ray photoelectron spectroscopy (XPS, ESCALAB 250Xi, America) was used to assess surface chemistry of BCF. The O_2 -temperature-programmed desorption (O_2 -TPD) of BCF were performed by an automatic chemical adsorption instrument (ChemStar-TPx, America).

To evaluate the electrochemical performance of RPCCs, the current-voltage (I-V, linear sweep rate of 20 mV s^{-1} from 0.4 V to open circuit voltage (OCV) in the FC mode and from OCV to 1.5 V in the EC mode and electrochemical impedance spectra (EIS) were characterized using an electrochemical workstation (BioLogic SP-300, France). In the FC mode, the flow rate of H_2 on the fuel electrode side and dry air on the air electrode side were 30 mL min^{-1} and 100 mL min^{-1} , respectively. In the EC mode, the flow rate of H_2 on the fuel electrode side and air with different content of water vapor on the air electrode side were 30 mL min^{-1} and 100 mL min^{-1} , respectively. For the impedance measurement, the frequency range was set to be 0.1 Hz - 1 MHz with an AC amplitude of 10 mV . The distribution of relaxation time (DRT) method was used to analyze the EIS data. The outlet gas of fuel electrode was analyzed by gas chromatograph (GC, 9790 plus, Zhejiang FULI Analytical Instrument Co., Ltd., China) to measure Faradic efficiencies (FEs, the ratio of the experimental and theoretical amount of H_2 produced at fixed current densities).

2.4. Distribution of relaxation time (DRT) and density functional theory (DFT)

The software used for distribution of relaxation time (DRT) analysis in this work is MATLAB, the same as the relevant literature [29]. The DRT results consist of the relaxation time distribution function $\gamma(\tau)$ and the corresponding relaxation time τ (tau). Bayesian analysis, peak analysis, and data quality certification used in this work are basically consistent with the relevant literatures [30,31].

Density functional theory (DFT)-based calculations was employed to further understand the ORR/OER activity using the Gaussian plane wave (GPW) method implemented in CP2K-2022.1 Quickstep module [32]. The exchange-correlation energy was described by the generalized-gradient approximation with spin-polarized Perdew-Burke-Ernzerh functional. A mixed plane wave with 65 Ry cutoff and the DVFP basis set with 1400 Ry cutoff. The core electrons were described by Goedecker-Teter-Hutter (GTH) pseudopotential. The energy convergence for the self-consistent field (SCF) calculation was set to be 5×10^{-6} Hartree. The maximum force on atomic was convergence in 4.5×10^{-4} Hartree/Bohr for geometry optimization. A supercell of $3 \times 3 \times 3$ unit cells of $\text{Ba}_{1-x}\text{Ca}_x\text{FeO}_{3-\delta}$ ($x=0.1, 0.2$, and 0.3) were used for calculation and the doping elements were replaced based on stoichiometric proportion. The spin polarization and electronic smearing were used in calculations.

3. Results and discussion

3.1. Phase structure

Fig. 2b shows the XRD patterns of $\text{Ba}_{1-x}\text{Ca}_x\text{FeO}_{3-\delta}$ ($x=0.0, 0.1, 0.2, 0.3$, BCF) oxides after firing at 1000°C for 5 h. The BCF oxides demonstrate an orthorhombic structure at $x=0$ and a cubic structure at $x=0.1, 0.2$, and 0.3 . A magnified view of the (110) crystal plane is shown in Fig. 2c. It can be seen that the peak position shifts to larger angles with

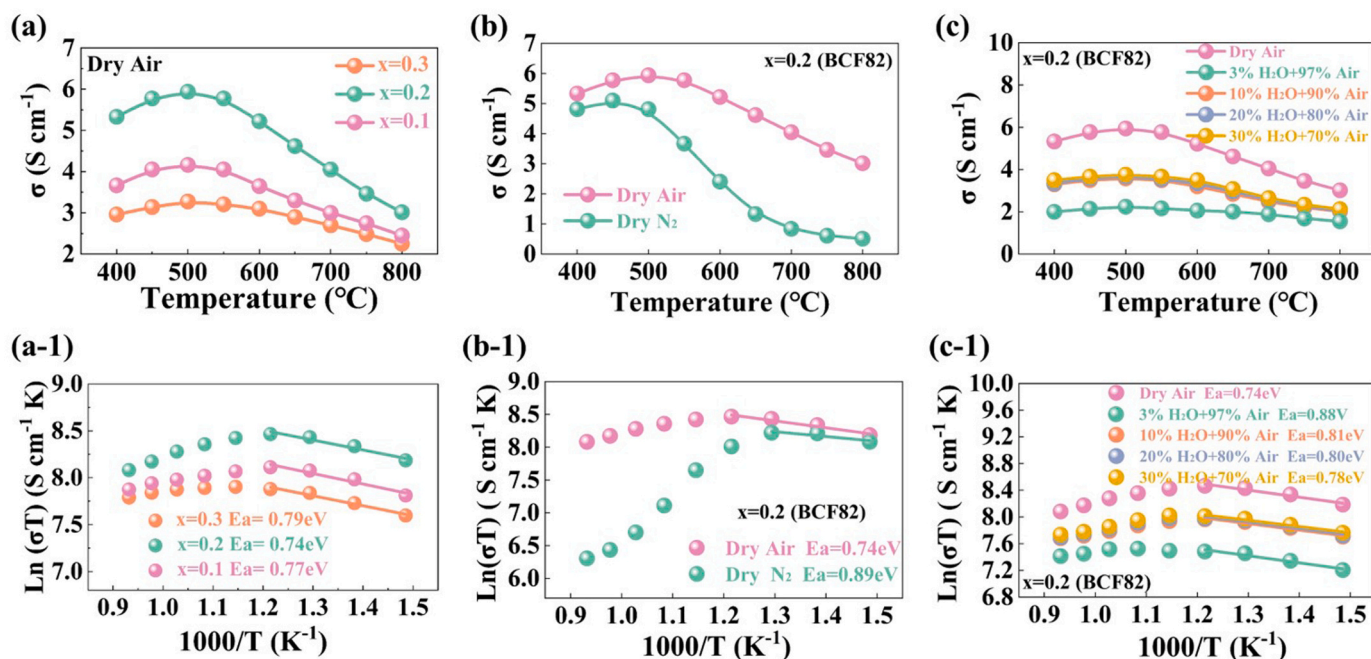


Fig. 3. Temperature dependence of electrical conductivity of (a) BCF oxides in dry air, (b) BCF82 oxides in dry Air and N₂, and (c) BCF82 oxides in air with 0%–30% H₂O; The corresponding Arrhenius plot of (a-1) dry air, (b-1) BCF82 oxides in dry Air and N₂, and (c-1) BCF82 oxides in air with 0%–30% H₂O.

the increase of Ca content, indicating a smaller lattice parameter and cell volume as increasing the Ca substitution. This is attributed to the smaller ionic radius of Ca²⁺ (1.00 Å) as compared with Ba²⁺ (1.42 Å). The XRD refinement results of the BCF oxides are shown in Fig. 2d for the BCF82 oxide and in Fig. S1 (Supporting Information) for the BCF91 and BCF73 oxides. The results suggest that all the BCF oxides can be assigned to a space group with Pm-3m (BCF91, a=b=c=4.0365 Å; BCF82, a=b=c=4.0333 Å; BCF73, a=b=c=4.0277 Å). Despite the small peaks at about 27.98° and 32.72°, which belongs to BaFe₂O₄, a cubic perovskite structure was formed for all the compositions. The lattice parameters of BCF oxides decrease significantly as increasing the doping level of Ca, suggesting the successful doping of Ca into the BaFeO₃ lattice through the sol-gel process. Fig. S2 in Supporting Information shows the XRD patterns of Ba_{0.8}Ca_{0.2}FeO_{3-δ} (BCF82), BZCYYb, and the BCF82-BZCYYb mixture (mass ratio of 1:1, after calcining at 1200 °C for 10 h). There are only diffraction peaks of BCF82 and BZCYYb, no additional peaks are observed, indicating the good chemical compatibility between BCF82 and BZCYYb electrolyte.

The high-resolution TEM (HR-TEM) image and the selected-area electron diffraction (SAED) of the BCF82 sample are shown in Fig. 2e. A lattice spacing of 0.284 nm is observed, which corresponds to the (110) plane of the perovskite structure. In addition, the (110) plane of BCF82 is also found in the SAED. The elemental distributions of BCF82 were further examined by the high-angle annular dark-field (HAADF) scanning transmission electron microscope (STEM), combined with the X-ray energy dispersive spectrum (EDS). As shown in Fig. 2f, the elements of Ba, Ca, Fe, and O are uniformly distributed. The above results indicate that the BCF82 with desired structure and composition has been successfully fabricated.

3.2. Conductivity analysis

Triple (e⁻/O²⁻/H⁺) conducting oxides have become superior candidates as the air electrode for protonic ceramic cells because of the introduction of proton conductivity, thus allowing the active reaction sites extending from the air electrode-electrolyte interface to the whole air electrode surface. Herein, the conductivities of Ba_{1-x}Ca_xFeO_{3-δ} (x=0.1, 0.2, 0.3, BCF) were measured by DC four-probe method at

400–800 °C and the conductivity calculation formula is supplied as Supporting Information. Fig. 3a shows the conductivities of Ba_{0.9}Ca_{0.1}FeO_{3-δ} (BCF91) with the density of 90.54%, Ba_{0.8}Ca_{0.2}FeO_{3-δ} (BCF82) with the density of 91.28%, and Ba_{0.7}Ca_{0.3}FeO_{3-δ} (BCF73) with the density of 91.78% measured in dry air. It can be seen that the conductivities of BCF firstly increase and then decrease as the Ca doping content increasing. The conductivities of BCF oxides exhibit a descending order: BCF82 > BCF91 > BCF73. Given that the concentration of carriers and the content of oxygen vacancies make an opposite contribution to conductivity. The BCF82 shows the highest conductivity of 5.94 S cm⁻¹ at 500 °C in dry air. The conductivity shows an increase from 400 to 500 °C because of the increased oxygen vacancy formation energy and ion mobility, which displays semiconductor-like properties. When the temperature exceeds 500 °C, the conductivity of BCF oxides decreases as the temperature increases. This phenomenon might be caused by the transformation of Fe⁴⁺ into Fe³⁺ in the lattice, which would reduce the carrier concentration at high temperatures [33,34]. The conductivity of BCF82 measured in N₂ is lower than that under dry air conditions as shown in Fig. 3b, which might be due to the reduced oxygen-ion conductivity under an inert atmosphere. Similarly, the conductivity of BCF82 is higher than that of BCF91 and BCF73 in the N₂ atmosphere (Fig. S3a in Supporting Information). It can be seen that the conductivity of BCF82 in wet air (3% H₂O, 10% H₂O, 20% H₂O, and 30% H₂O) is lower than that under dry air conditions, as shown in Fig. 3c, which might be caused by the introduction of protons that consumed part of the electron holes [35,36]. And BCF82 oxides also present the similar conductivity variations in different steam concentrations as it does in dry air atmosphere due to its semiconductor-like properties at low temperature (< 500 °C) and metal-like properties at high temperature (> 500 °C). Furthermore, the electrical conductivity of BCF82 shows a decrease at 400–800 °C from dry to 3% H₂O air and then significantly increase from 3% H₂O to high H₂O steam concentration (10% H₂O, 20% H₂O, and 30% H₂O), while only slightly increase is observed in BCF82 oxide from 10% H₂O to 30% H₂O content, which may be attributed to the improved hydration capacity of the material in high steam concentration [37]. The decreased total conductivity at 3% H₂O air may be caused by the decreased hole concentration as other reports [38,39]. BCF91 and BCF73 also exhibit the same conductivity variations in

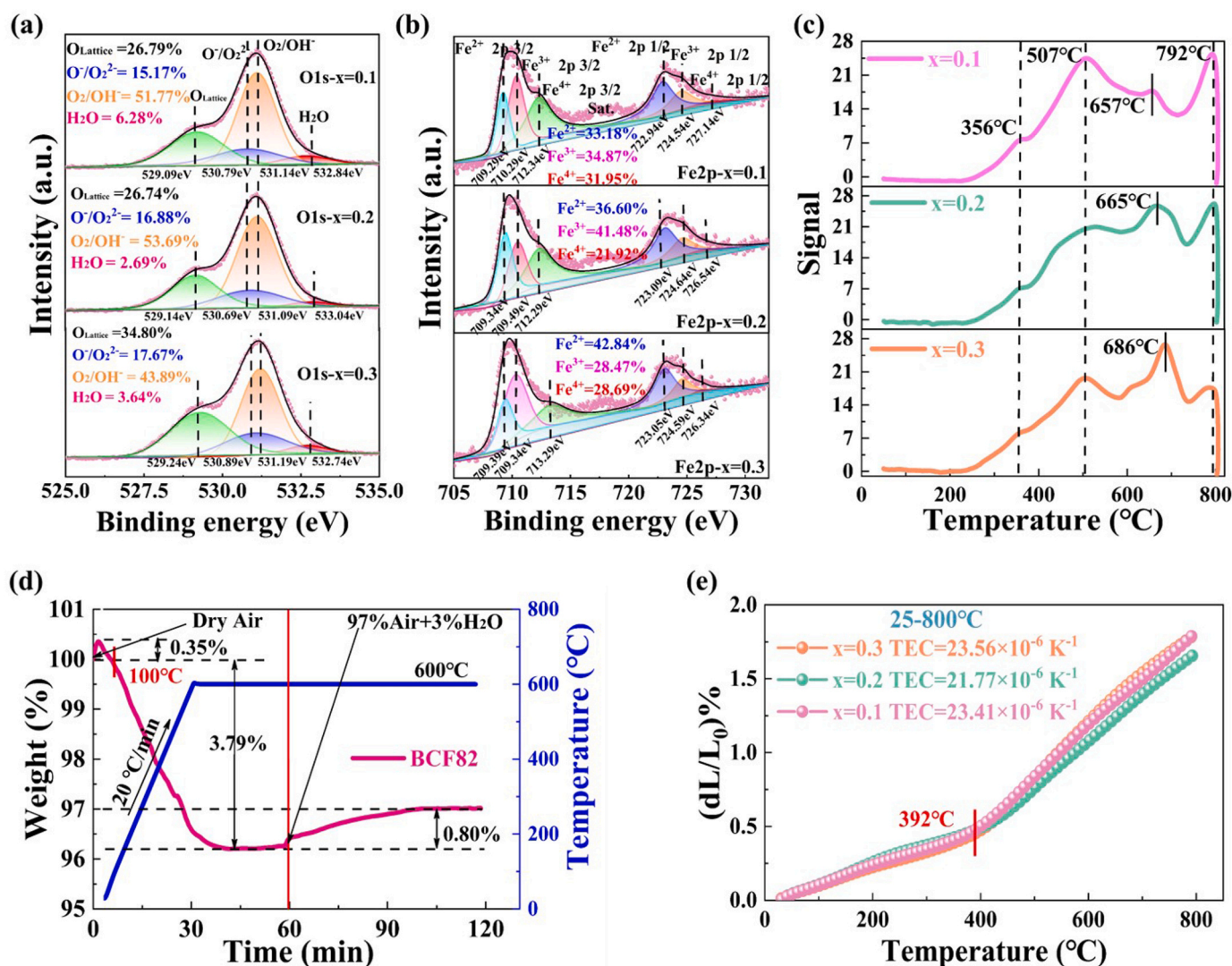


Fig. 4. Characteristic analysis of BCF oxides. (a) XPS analysis of O 1s; (b) XPS analysis of Fe 2p; (c) O₂-TPD curves of BCF oxides; (d) TGA analysis of BCF82; (e) Thermal expansion of BCF oxides.

different steam concentrations (Fig. S3b and Fig. S3c in Supporting Information). Additionally, the corresponding Arrhenius diagrams of conductivities of BCF in dry air, N₂, and wet air are shown in Figs. 3 (a-1), 3(b-1), and 3(c-1). The activation energy (E_a) of BCF91, BCF82, and BCF73 was 0.77, 0.74, and 0.79 eV, respectively, indicating a lowest E_a for BCF82 (Figs. 3(a-1)). In contrast, BCF82 shows larger E_a values of 0.89 eV, 0.88 eV, 0.81 eV, 0.80 eV, and 0.78 eV in dry N₂ and wet air with 3% H₂O, 10% H₂O, 20% H₂O, and 30% H₂O, respectively.

3.3. Absorption, hydration, and thermal properties

Since oxygen vacancies act as both pathways for ionic transport and active sites for electrochemical processes, they are essential in defining the catalytic activity of air electrodes. As shown in Fig. 4a, the O 1s XPS spectra of BCF could be fitted into four peaks, attributing to lattice oxygen (O_{Lattice}), highly oxidative oxygen species ($O^{\cdot}/O_2^{\cdot-}$), adsorbed oxygen/hydroxide groups (O_2/OH^{\cdot}), and adsorbed water (H_2O) from the low binding energy to high binding energy. Lattice oxygen (O_{Lattice}) of BCF91, BCF82, and BCF73 accounted for 26.79%, 26.74%, and 34.80% of the total oxygen species, respectively. Notably, the oxygen vacancy content is a significant indicator for the oxygen activation capacity of the catalyst, which is directly positively correlated with the amount of the highly oxidative oxygen species ($O^{\cdot}/O_2^{\cdot-}$) in the sample [40,41]. It

can be seen that the relative concentration of the adsorbed oxygen species ($O^{\cdot}/O_2^{\cdot-}$) increases as Ca doping content increasing. This result shows that Ca doping facilitates the formation of oxygen vacancies [42]. Furthermore, three kinds of Fe cations (Fe^{2+} , Fe^{3+} , and Fe^{4+}) fitted into six peaks are shown in Fig. 4b. As can be seen, the Fe 2p spectra of BCF91, BCF82, and BCF73 oxides with percentages of Fe^{4+} are 31.95%, 21.92%, and 28.69%, respectively; of Fe^{3+} are 34.87%, 41.48%, and 28.47%, respectively; and of Fe^{2+} are 33.18%, 36.60, and 42.84%, respectively. Consequently, the average ionic valence for the B-site decreases as Ca doping content increases, which leads to the increased oxygen vacancy concentration [43].

The oxygen adsorption capacity of the material is also an important index for the activity of the air electrode. As shown in Fig. 4c, oxygen desorption ability is characterized by O₂-temperature-programmed desorption (O₂-TPD). Four desorption peaks are observed for the BCF oxide. The former two peaks around 300–550 °C can be ascribed to the α -oxygen desorption, coming from the chemisorbed oxygen desorption on the surface (α_1 -O₂) and the lattice oxygen loss (α_2 -O₂) [33,44]. At this temperature, the unstable Fe^{4+} ions are reduced to the Fe^{3+} ones, while the lattice oxygen diffuses from the bulk to the surface via the oxygen vacancy defects. The last two peaks at 550–800 °C are referred as β -oxygen desorption, which are related to the liberation of O₂ from the lattice [45]. The peaks intensity of BCF oxides exhibit a descending

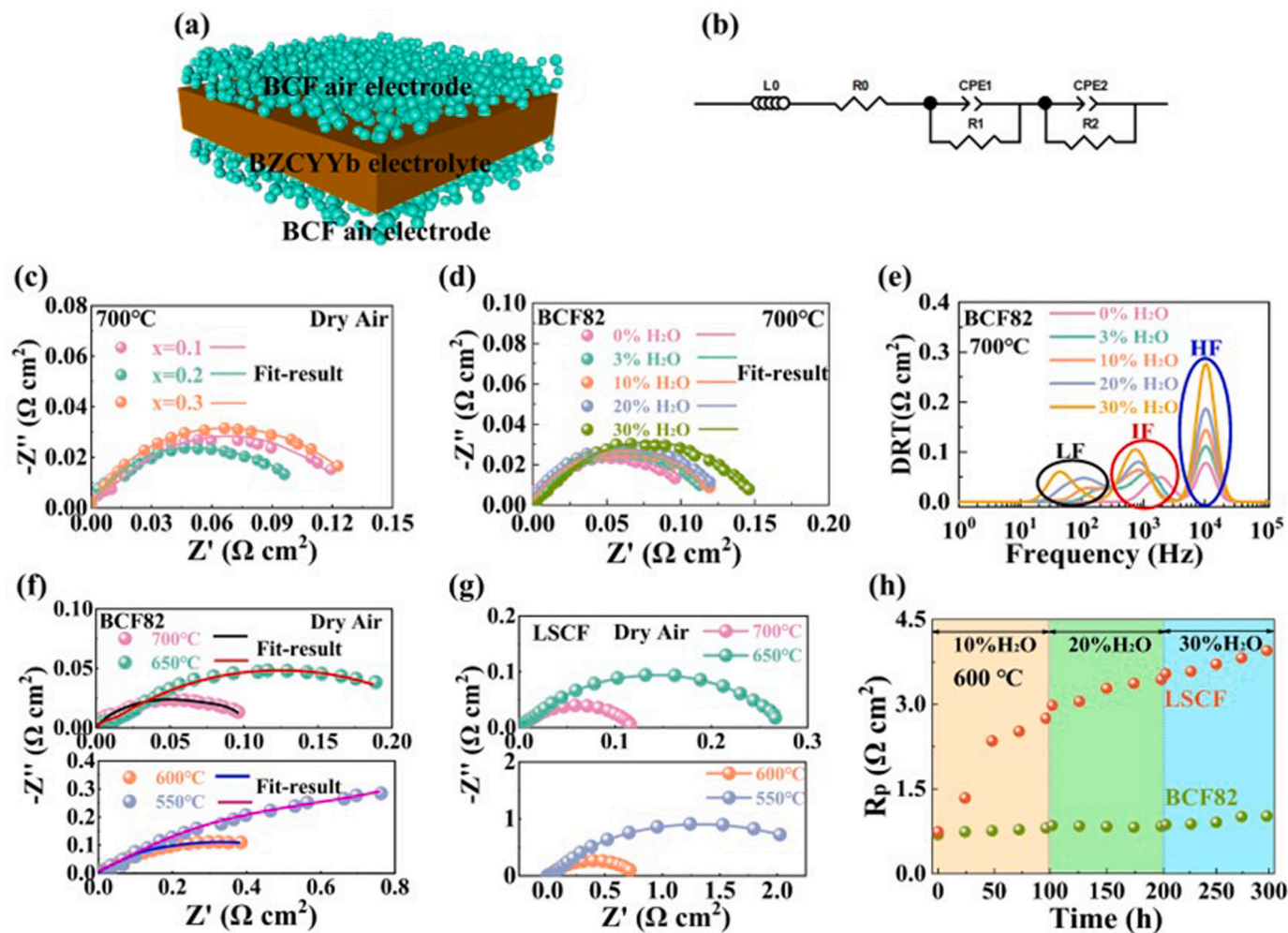


Fig. 5. (a) Schematic illustration of the symmetrical cell; (b) The equivalent circuit model for EIS fitting; (c) EIS of the BCF air electrodes measured at 700 °C in dry air; (d) EIS of the BCF82 air electrode measured in air with 0%–30% H₂O; (e) The corresponding DRT plots of the EIS shown Fig. 5(d); EIS of (f) the BCF82 air electrode, and (g) the LSCF air electrode measured in dry air at 700–550 °C; (h) Time dependence of R_p of the symmetrical cells with the BCF82 and LSCF electrodes measured in wet air at 600 °C under open-circuit conditions.

order: BCF82 > BCF91 > BCF73, revealing the highest oxygen desorption capability of BCF82.

To understand the proton conducting ability of the air electrode material, thermogravimetric analysis (TGA) was performed to characterize the hydration capability of BCF82. As shown in Fig. 4d, the TG profile in dry air (0–60 min) and in humid air (60–120 min) is plotted. In dry air, a small weight gain at the temperature below 50 °C is shown, which may be caused by the adsorption of surface species, such as moisture and carbon dioxide. Subsequently, a weight loss between 50 and 100 °C is shown. Then the weight loss of 3.79 wt% appears at the temperature range of 100–600 °C, which is ascribed to the release of lattice oxygen to form oxygen vacancies [46]. As switching the atmosphere from dry air to humid air, a weight gain of 0.80 wt% is observed at 600 °C, which may be related to the hydration reaction [47]. The proton conduction of BCF is mainly through the hydration reaction (Eq. (1)) and hydrogenation reaction (Eq. (2)) [10]. In addition, the variation of weight as a function of temperature for the BCF82 oxide in air was further investigated and shown in Fig. S4 (Supplementary Information). There is a small peak between 360 and 400 °C, which may be caused by the formation of oxygen vacancies.



Where $\text{V}_\text{O}^{\bullet\bullet}$, $\text{O}_\text{O}^{\times}$, $\text{OH}_\text{O}^{\bullet}$, and h^{\bullet} represent oxygen vacancy, lattice oxygen, hydroxide ion occupying oxygen sites, and electron holes, respectively.

The thermal expansion curves of the BCF samples in air are shown in Fig. 4e. An inflection point at around 392 °C is observed, which may be ascribed to the reduction of Fe^{4+} to Fe^{3+} and the release of lattice oxygen, resulting in the formation of extrinsic oxygen vacancies [33], which is consistent with the experimental results of Fig. S4 (Supplementary Information). The average thermal expansion coefficients (TECs) of BCF are $23.41 \times 10^{-6} \text{ K}^{-1}$, $21.77 \times 10^{-6} \text{ K}^{-1}$, and $23.56 \times 10^{-6} \text{ K}^{-1}$ for $x=0.1$, 0.2, and 0.3 between 25 °C and 800 °C, respectively. It is worth noting that the TEC of BCF82 is lower than that of the perovskites containing Co, such as $\text{PrBa}_{0.8}\text{Sr}_{0.2}\text{Co}_2\text{O}_{6-\delta}$ ($25.9 \times 10^{-6} \text{ K}^{-1}$ at 300–800 °C) [8], $\text{PrBaCo}_2\text{O}_{5+\delta}$ ($23.74 \times 10^{-6} \text{ K}^{-1}$ at 25–1000 °C) [46], $\text{PrBaCo}_{1.95}\text{Sc}_{0.05}\text{O}_{5+\delta}$ ($23.6 \times 10^{-6} \text{ K}^{-1}$ at 30–1000 °C) [48], and $\text{NdBa}_{0.5}\text{Sr}_{0.5}\text{Co}_2\text{O}_{5+\delta}$ ($25.4 \times 10^{-6} \text{ K}^{-1}$ at 150–800 °C) [49]. Hence, it is suggested that the BCF82 oxide has relatively closer TEC with proton conducting electrolytes ($\text{BaZr}_{0.80}\text{Y}_{0.20}\text{O}_{3-\delta}$, $8.2 \times 10^{-6} \text{ K}^{-1}$ at 100–900 °C [50]; $\text{BaZr}_{0.60}\text{Ce}_{0.2}\text{Y}_{0.2}\text{O}_{3-\delta}$, $9.1 \times 10^{-6} \text{ K}^{-1}$ at 100–900 °C [50]; $\text{BaZr}_{0.1}\text{Ce}_{0.7}\text{Y}_{0.2}\text{O}_{3-\delta}$, $10.1 \times 10^{-6} \text{ K}^{-1}$ at 25–1000 °C [51] and $\text{BaZr}_{0.1}\text{Ce}_{0.7}\text{Y}_{0.1}\text{Yb}_{0.1}\text{O}_{3-\delta}$, $11.8 \times 10^{-6} \text{ K}^{-1}$ at 25–750 °C [28]) compared with other Co-based air electrode materials.

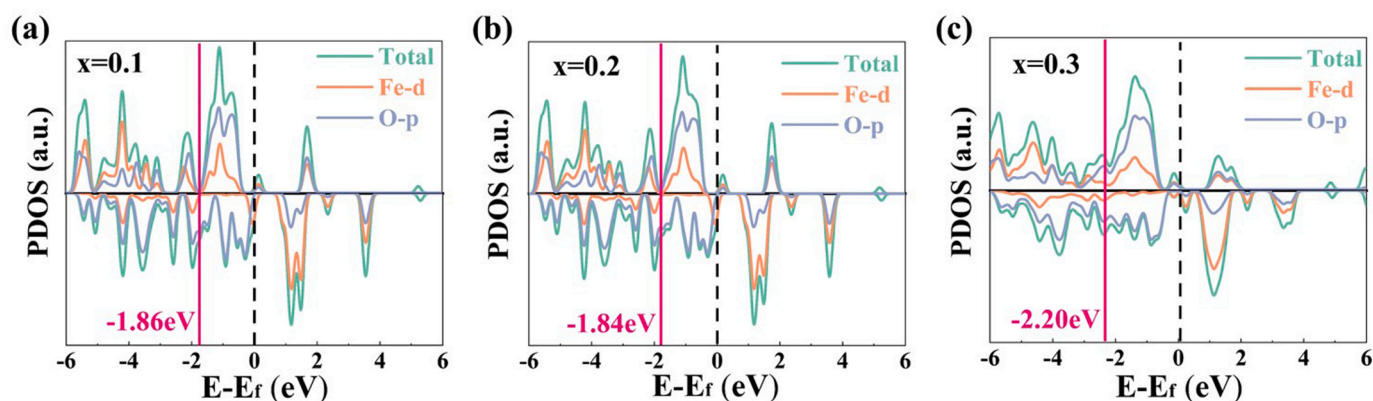


Fig. 6. Electronic PDOS of BCF oxides. (a) $x=0.1$, (b) $x=0.2$, and (c) $x=0.3$.

3.4. Analysis of symmetrical cells

To better understand the catalytic activity of the BCF air electrode, electrochemical impedance spectra (EIS) curves of BZCYYb-supported symmetrical cells with the BCF air electrode are evaluated. Fig. 5a and b show the schematic illustration of the symmetrical cell and the equivalent circuit model for EIS fitting, respectively. The L_0 corresponds to an inductance, R_0 is related to the ohmic impedance, CPE1 and CPE2 represent the constant phase element, R1 and R2 correspond to different electrode polarization impedance. Fig. 5c illustrates the EIS curves of symmetrical $\text{Ba}_{1-x}\text{Ca}_x\text{FeO}_{3-\delta}$ ($x=0.1, 0.2$, and 0.3 , BCF) air electrodes measured at 700°C in dry air. The BCF82 air electrode shows the lowest polarization resistance (R_p) of $0.11 \Omega \text{ cm}^2$, as well as the lowest activation energy of 0.46 eV (shown in Fig. S5 in Supporting Information). To analyze the influence of steam content on the electrode performance, EIS of symmetrical cells with a BCF82 air electrode were measured at 700°C in dry and wet air (including 3%, 10%, 20%, and 30% H_2O) and shown in Fig. 5d. It can be seen that the lowest R_p is observed in dry air and the R_p value of the BCF82 electrode increases with increasing the H_2O content. Similar trend on BCF91 and BCF73 symmetrical cells can be observed in Fig. S6 in Supporting Information. The increased R_p in wet air might be explained by the adsorption of H_2O molecules and the reduced O_2 concentration on the surface of the BCF electrode, which resulted in decreased active sites for O_2 adsorption and dissociation, and the reduced mass transfer process [49]. To get a better understanding of the rate-determining step of the electrochemical reactions in the air electrode, distribution of relaxation time (DRT) was used to analyze EIS of the BCF82 air electrode [52,53]. As displayed in Fig. 5e, the DRT plots can be divided into three peaks based on the frequency range, including high frequency (HF), intermediate frequency (IF), and low frequency (LF), respectively. The HF peak is ascribed to charge transfer process (the transfer of ions from electrolyte to electrode in the triple phase boundary), IF peak is related to gas (steam and O_2) surface exchange and ionic (O^{2-} and H^+) bulk diffusion, and the LF peak is associated with gas diffusion within the electrode [7,12,54]. The electrochemical processes at HF, IF, and LF ranges show negative dependence on the variation of H_2O contents. The integral areas of all frequency ranges increase with the increase of the H_2O content, due likely to the deteriorated gas diffusion, surface O_2 exchange, and charge transfer processes under a higher steam concentration [55].

In addition, EIS of symmetrical cells with the BCF82 and LSCF air electrode measured at $700\text{--}550^\circ\text{C}$ in dry air are shown in Fig. 5f and Fig. 5g, respectively. The BCF82 air electrode shows higher activity than LSCF. In addition, the BCF82 air electrode shows a slightly lower activation energy (E_a) of 0.99 eV than that of the LSCF air electrode (1.20 eV) (Fig. S4a). Fig. S7a and Table S1 (Supporting Information) compare the R_p of recently developed high-performance Co-free air electrodes [56–61], demonstrating the high catalytic activity of the

BCF82 air electrode. Fig. 5h further shows the stability of the BCF82 and LSCF symmetrical cells under different steam concentrations. Excellent stability of the BCF82 air electrode in high concentrations of steam is observed compared to that of the LSCF air electrode. The degradation rate of R_p for the BCF82 is much lower than that of the LSCF electrode, which is 1.11×10^{-3} and $1.01 \times 10^{-2} \Omega \text{ cm}^2 \text{ h}^{-1}$, respectively at 600°C under 10%–30% H_2O for the total 300 h measurement. It has been reported that the stability of LSCF air electrodes is significantly affected by the Sr segregation [9,62,63]. The evolution of the EIS of the BCF82 and LSCF air electrodes during the stability test are shown in Fig. S7b and Fig. S7c in Supporting Information, respectively. Furthermore, DRT analysis was employed to deconvolute the EIS spectra of the BCF82 and LSCF air electrodes (Fig. S7d and Fig. S7e in Supporting Information). The mainly increased DRT area in the LF range during the stability test is likely due to the deteriorated surface reaction activity.

3.5. DFT-based calculations

The electronic density of states (DOS) is normally utilized as the descriptors correlated to the ORR/OER activity [64]. As shown in Fig. 6, the strong hybridization among the Fe-3d and O-2p orbitals exists in the energy range of partial electronic density of states (PDOS), which crosses the Fermi level. Therefore, the electrons can easily hop along $\text{Fe}^{3+} \rightarrow \text{O}^{2-} \rightarrow \text{Fe}^{4+} \rightarrow \text{O}^{2-} \rightarrow \text{Fe}^{3+}$, implying the existence of oxygen vacancies in the BCF oxides [65]. The O partial DOS and O-p band centers of BCF oxides are -1.86 , -1.84 and -2.20 eV for BCF91, BCF82, and BCF73, respectively. It shows that BCF82 has a lower O-p band center value and is closer to the Fermi level than that of BCF91 and BCF73, suggesting the higher ORR/OER activity of BCF82 [66], which is consistent with the experimental results as shown above.

3.6. Electrochemical performance of RPCCs

Fuel electrode-supported cells with a configuration of Ni-BZCYYb/BZCYYb/BCF were prepared and tested to further evaluate the performance and stability of the BCF air electrodes. Fig. 7a shows a cross-sectional SEM image of the single cell with a porous NiO-BZCYYb fuel electrode, a dense BZCYYb electrolyte ($\approx 10 \mu\text{m}$ in thickness), and a porous BCF82 air electrode. The EIS and typical current density-voltage-power density (I-V-P) of the RPCC with a BCF82 air electrode in the fuel cell operation mode (under H_2 /dry air atmospheres) are shown in Fig. 7b and Fig. 7c, respectively. The R_0 values are 0.085 , 0.11 , and $0.13 \Omega \text{ cm}^2$, while the R_p values are 0.11 , 0.18 , and $0.33 \Omega \text{ cm}^2$ at 700 , 650 and 600°C , respectively. Peak power densities (PPDs) of the cell are 1.14 , 0.98 , and 0.73 W cm^{-2} at 700 , 650 , and 600°C , respectively, which are higher than those of the cells with the BCF91 and BCF73 air electrodes (shown in Fig. S8), consisting with the symmetrical cell results. The details of the comparison of R_0 , R_p , OCV, and PPD of fuel cells

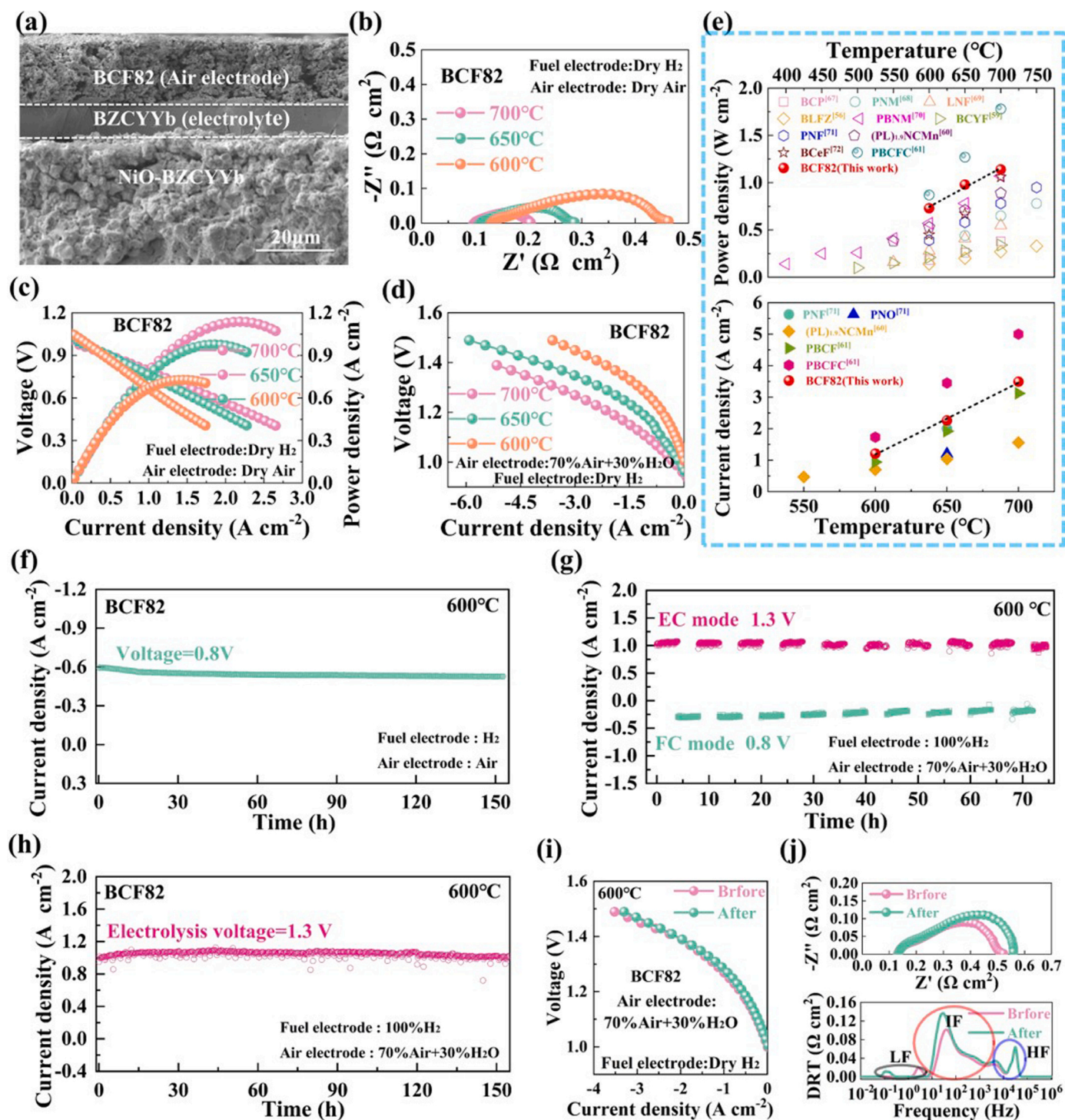


Fig. 7. Electrochemical performance of RPCCs with a BCF82 air electrode. (a) Typical cross-sectional SEM image of a single-cell before the electrochemical test; (b) Typical EIS curves of the cell measured at 600–700 °C under OCV conditions; (c) I-V-P curves of the cell measured in the FC mode at 600–700 °C; (d) Typical I-V curves of the cell measured in the EC mode at 600–700 °C; (e) Comparison of the PPDs in the FC mode (top) and current densities at 1.3 V in the EC mode (bottom) of the cell with a BCF82 and other recently reported cells with Sr and Co-free air electrodes; (f) Stability of the RPCC measured in the FC mode (at a constant voltage of 0.8 V); (g) Cyclic operational stability of the RPCC between the fuel cell and electrolysis modes; (h) Stability of the cell measured in the EC mode at 1.3 V under H_2/air with 30% H_2O ; (i) I-V curves of the cell before and after the stability test in the EC mode; (j) EIS and corresponding DRT of the cell before and after the electrolysis stability test at 600 °C.

with BCF air electrodes measured at different temperatures can be found in Fig. S9 (Supporting Information).

RPCCs with the BCF air electrodes were also measured in the electrolysis mode. I-V and EIS of the electrolysis cell with a BCF82 air electrode are shown in Fig. 7d and Fig. S10a (Supporting Information),

respectively. Electrochemical performance of the cells with the BCF91 and BCF73 air electrodes are shown in Fig. S10b-S10e (Supporting Information). As shown in Fig. 7d, the electrolysis current densities of the cell with a BCF82 air electrode are 3.49, 2.26, and 1.21 A cm^{-2} at an applied voltage of 1.3 V under H_2/air with 30% H_2O at 700, 650, and

600 °C, respectively. The electrolysis performances are significantly higher than those of the cells with the BCF91 and BCF73 air electrodes (Fig. S10 in Supporting Information), demonstrating the superior OER activity of the BCF82 air electrode. The RPCC with a BCF82 air electrode exhibits the lowest R_p values (seen re-plots of the R_o , R_p , OCV and current densities at 1.3 V of RPCCs with BCF air electrodes measured in the electrolysis mode at different temperatures in Fig. S11), confirming the superior OER activity of the BCF82 air electrode. The steam concentration dependence of the performance of the electrolysis cell with a BCF82 air electrode was further measured at 650 °C. As shown in Fig. S12 in Supporting Information, minimal impact on the electrochemical characteristics of the electrolysis cell is observed when varying the H_2O from 10% to 30% [23]. The comparison of the PPDs in the FC mode (Fig. 7e, top) and current densities (at 1.3 V) in the EC mode (Fig. 7e, bottom) of the RPCCs with a BCF82 air electrode and other recently reported Sr and Co-free air electrodes are summarized [56, 59–61, 67–72]. As shown, the performances of our cells with the BCF82 air electrode are significantly higher than those of other Sr and Co-free air electrodes (e.g., $PrBa_{0.8}Ca_{0.2}Fe_{2}O_{6-\delta}$ [61], $Pr_2NiO_{3.9+6}F_{0.1}$ [71], $Ba_{0.36}Ce_{0.64}FeO_{3-\delta}$ [72] et al.), except for the cell with the $PrBa_{0.8}Ca_{0.2}Fe_{1.8}Ce_{0.2}O_{6-\delta}$ air electrode, with an excellent peak power density of 1.78 W cm^{-2} in the FC mode and a high current density of 5 A cm^{-2} under 1.3 V in the EC at 700 °C. This great improvement over our BCF electrode may be due to the extra generated $BaCeO_3$ and CeO_2 particles on the electrode (the thickness of the BZCYYb electrolyte is same with 10 μm), which can enhance the conduction/transfer of protons and oxygen ions and provide more active sites for oxygen reactions [61]. The detailed lists of the cell operation conditions and performance in the FC and EC modes are provided in Tables S2 and S3 in Supporting Information.

Furthermore, the durability of the cell with a BCF82 air electrode was evaluated in different operating modes at 600 °C. When operated in the FC mode, the cell shows a stable current density of 0.54 A cm^{-2} during the 150 h test despite the slight degradation in the initial 15 h (Fig. 7f). In addition, the RPCC exhibits excellent reversibility during the cycling test between the FC (0.8 V) and EC (1.3 V) modes (Fig. 7g). Furthermore, the RPCC shows a relatively stable operation in the EC mode at a cell voltage of 1.3 V with 30% H_2O in air over 150 h (Fig. 7h). Fluctuations in the curve may be caused by the unstable steam supply. Furthermore, the Faraday efficiencies (FEs) of RPCCs were evaluated at 600 °C based on the ratio of the experimental and theoretical hydrogen generation rates. As shown in Fig. S13 (Supporting Information), the FE of the electrolysis cell with a BCF82 electrode is 80% under 1.3 V with 30% steam at 600 °C, which is comparable to the reported results [73]. I-V and EIS of the RPCC measured in the EC mode before and after the stability test are shown in Fig. 7i and Fig. 7j (top), respectively. It can be seen that the R_o remains stable and the R_p of the cell shows an increase from $0.39\text{ }\Omega\text{ cm}^2$ to $0.42\text{ }\Omega\text{ cm}^2$, resulting in a decrease in the electrolysis current density from 1.27 A cm^{-2} to 1.21 A cm^{-2} at 1.3 V. As shown in Fig. 7j (bottom), the DRT analysis shows an increase in IF peak after the stability test, which could be caused by the decreased porosity of the air electrode [74].

In addition, the microstructure of the cell with a BCF82 air electrode after the stability measurement in the electrolysis mode is presented in Fig. S14a (Supporting Information). A dense BZCYYb electrolyte and good adhesion between the porous electrodes and the electrolyte layers are shown. Fig. S14b and S14c show the magnified view of the BCF82 air electrode before and after the stability test respectively, showing the reduced porosity and increased particles size of the air electrode after the stability test, leading to the slight degradation of the cell in the electrolysis mode as shown in Fig. 7h. Additionally, the EDS elemental mapping of the BCF82 air electrode after the stability test was measured. As shown in Fig. S15 in Supplementary Information, the elements of Ba, Fe, Ca, and O are uniformly distributed, indicating that the BCF82 air electrode has no segregation issue after the stability test.

4. Conclusions

A series of $Ba_{1-x}Ca_xFeO_{3-\delta}$ (BCF, $x=0.1, 0.2$ and 0.3) oxides were synthesized and employed as the air electrodes for RPCCs. The experimental results suggested that BCF showed good surface exchange and ionic (O^{2-}/H^+) bulk diffusion capability, ensuring both high ORR and OER activities satisfying the bi-functional requirements for RPCCs air electrodes. DFT-based calculations suggest that the excellent OER/ORR activity is attributed to the lower O-P band center value of the BCF82 oxide. Furthermore, RPCCs with the BCF82 air electrode showed high performance in both modes: achieving a peak power density of 1.14 W cm^{-2} in the fuel cell mode and a current density of 3.49 A cm^{-2} at 1.3 V in an electrolysis mode at 700 °C. Additionally, the cell demonstrated good durability in the fuel cell, electrolysis, and reversible modes at 600 °C for hundreds of hours without elemental segregation and delamination on the air electrode/electrolyte interface. These promising results highlight the great potential of BCF82 as an ideal air electrode material for RPCCs.

CRediT authorship contribution statement

Guangjun Zhang: Conceptualization, Data curation, Formal analysis, Investigation, Methodology, Validation, Writing original draft, Writing – review & editing. **Ting Chen:** Project administration, Validation, Funding acquisition, Writing – review & editing. **Yuechao Yao:** Investigation, Methodology. **Chenxiao Wang:** Validation, DFT calculation. **Xiaonan Bao:** review & editing. **Guozhu Zheng:** Data curation, Investigation. **Zuzhi Huang:** Data curation, Formal analysis. **Xiaoyu Zhang:** Data curation, Investigation. **Kui Liu:** Data curation, Investigation. **Lang Xu:** Validation, Funding acquisition. **Yucun Zhou:** Validation, Methodology, Writing – review & editing. **Shaorong Wang:** Resources, Supervision, Funding acquisition, Writing – review & editing.

Declaration of Competing Interest

The authors declare that they have no known competing financial interests or personal relationships that could have appeared to influence the work reported in this paper.

Data availability

Data will be made available on request.

Acknowledgement

The authors gratefully acknowledge the support of the National Key R&D Program of China (2021YFB4001502), National Natural Science Foundation of China (No. 52202334 and No. U2005215), and Science and Technology Innovation Foundation of Jiangsu Province for Carbon Neutrality (BK20220011).

Appendix A. Supporting information

Supplementary data associated with this article can be found in the online version at doi:10.1016/j.apcatb.2024.124176.

References

- [1] C.J. Davey, B. Luqmani, N. Thomas, E.J. McAdam, Transforming wastewater ammonia to carbon free energy: integrating fuel cell technology with ammonia stripping for direct power production, Sep. Purif. Technol. 289 (2022) 120755, <https://doi.org/10.1016/j.seppur.2022.120755>.
- [2] M.B. Hossain, M.R. Islam, K.M. Muttaqi, D. Sutanto, A.P. Agalgaonkar, Advancement of fuel cells and electrolyzers technologies and their applications to renewable-rich power grids, J. Energy Storage 62 (2023) 106842, <https://doi.org/10.1016/j.est.2023.106842>.

- [3] R. Wurster, J. Schindler, Solar and wind energy coupled with electrolysis and fuel cells, *Handb. Fuel Cells* (2010), <https://doi.org/10.1002/9780470974001.f31006>.
- [4] A. Kasaean, M. Javidmehr, M.R. Mirzaie, L. Fereidooni, Integration of solid oxide fuel cells with solar energy systems: a review, *Appl. Therm. Eng.* 224 (2023) 120117, <https://doi.org/10.1016/j.applthermaleng.2023.120117>.
- [5] M. Pan, W. Que, X. Li, Z. Wang, Y. Zeng, X. Zhou, A novel multi-generation energy harvesting system integrating photovoltaic and solid oxide fuel cell technologies, *J. Clean. Prod.* 425 (2023) 138770, <https://doi.org/10.1016/j.jclepro.2023.138770>.
- [6] J.-S. Shin, H. park, K. Park, M. Saqib, M. Jo, J. Kim, H.-T. Lim, M. Kim, J. Kim, J.-Y. Park, Activity of layered swedenborgite structured $\text{Y}_{0.8}\text{Er}_{0.2}\text{BaCo}_{3.2}\text{Ga}_{0.8}\text{O}_{7+\delta}$ for oxygen electrode reactions in at intermediate temperature reversible ceramic cells, *J. Mater. Chem. A* 9 (2020), <https://doi.org/10.1039/D0TA11000K>.
- [7] M. Liang, Y. Wang, Y. Song, D. Guan, J. Wu, P. Chen, A. Maradesa, M. Xu, G. Yang, W. Zhou, W. Wang, R. Ran, F. Ciucci, Z. Shao, High-temperature water oxidation activity of a perovskite-based nanocomposite towards application as air electrode in reversible protonic ceramic cells, *Appl. Catal. B: Environ.* 331 (2023) 122682, <https://doi.org/10.1016/j.apcatb.2023.122682>.
- [8] F. He, Y. Zhou, T. Hu, Y. Xu, M. Hou, F. Zhu, D. Liu, H. Zhang, K. Xu, M. Liu, Y. Chen, An efficient high-entropy perovskite-type air electrode for reversible oxygen reduction and water splitting in protonic ceramic cells, *Adv. Mater.* 35 (2023) 2209469, <https://doi.org/10.1002/adma.202209469>.
- [9] Y. Zhou, W. Zhang, N. Kane, Z. Luo, K. Pei, K. Sasaki, Y. Choi, Y. Chen, D. Ding, M. Liu, An efficient bifunctional air electrode for reversible protonic ceramic electrochemical cells, *Adv. Funct. Mater.* 31 (2021) 2105386, <https://doi.org/10.1002/adfm.202105386>.
- [10] N. Wang, C. Tang, L. Du, R. Zhu, L. Xing, Z. Song, B. Yuan, L. Zhao, Y. Aoki, S. Ye, Advanced cathode materials for protonic ceramic fuel cells: recent progress and future perspectives, *Adv. Energy Mater.* 12 (2022) 2201882, <https://doi.org/10.1002/aenm.202201882>.
- [11] S. Dila Safian, N. Izzati Abd Malek, N. Osman, Microstructure and electrochemical properties of modified LaSrCoFeO_3 cathode thin film on proton conductor ceramics, *Mater. Today.: Proc.* 66 (2022) 4033–4035, <https://doi.org/10.1016/j.matpr.2022.05.336>.
- [12] Z. Liu, Y. Chen, G. Yang, M. Yang, R. Ji, Y. Song, R. Ran, W. Zhou, Z. Shao, One-pot derived thermodynamically quasi-stable triple conducting nanocomposite as robust bifunctional air electrode for reversible protonic ceramic cells, *Appl. Catal. B: Environ.* 319 (2022) 121929, <https://doi.org/10.1016/j.apcatb.2022.121929>.
- [13] D.H. Kim, S. Yang, D.-H. Kwon, H.-I. Ji, J.-W. Son, J.H. Shim, Improved strontium segregation suppression of lanthanum strontium cobalt oxide cathode via chemical etching and atomic layer deposition, *Int. J. Energy Res.* 46 (2022) 12467–12475, <https://doi.org/10.1002/er.8012>.
- [14] S.D. Safian, N.I. Abd Malek, Z. Jamil, S.-W. Lee, C.-J. Tseng, N. Osman, Study on the surface segregation of mixed ionic-electronic conductor lanthanum-based perovskite oxide $\text{La}_{1-x}\text{Sr}_x\text{Co}_{1-y}\text{Fe}_y\text{O}_{3-\delta}$ materials, *Int. J. Energy Res.* 46 (2022) 7101–7117, <https://doi.org/10.1002/er.7733>.
- [15] S.J. Yang, W. Chang, H.J. Jeong, D.H. Kim, J.H. Shim, High-performance protonic ceramic fuel cells with electrode-electrolyte composite cathode functional layers, *Int. J. Energy Res.* 46 (2022) 6553–6561, <https://doi.org/10.1002/er.7591>.
- [16] J. Kim, A. Jun, O. Gwon, S. Yoo, M. Liu, J. Shin, T.-H. Lim, G. Kim, Hybrid-solid oxide electrolysis cell: A new strategy for efficient hydrogen production, *Nano Energy* 44 (2018) 121–126, <https://doi.org/10.1016/j.nanoen.2017.11.074>.
- [17] M. Choi, S.J. Kim, W. Lee, Effects of water atmosphere on chemical degradation of $\text{PrBa}_{0.5}\text{Sr}_{0.5}\text{Co}_{1.5}\text{Fe}_{0.5}\text{O}_{5+\delta}$ electrodes, *Ceram. Int.* 47 (2021) 7790–7797, <https://doi.org/10.1016/j.ceramint.2020.11.124>.
- [18] M. Liang, Y. Song, D. Liu, L. Xu, M. Xu, G. Yang, W. Wang, W. Zhou, R. Ran, Z. Shao, Magnesium tuned triple conductivity and bifunctionality of $\text{BaCo}_{0.4}\text{Fe}_{0.4}\text{Zr}_{0.1}\text{Y}_{0.1}\text{O}_{3-\delta}$ perovskite towards reversible protonic ceramic electrochemical cells, *Appl. Catal. B: Environ.* 318 (2022) 121868, <https://doi.org/10.1016/j.apcatb.2022.121868>.
- [19] K. Wei, N. Li, Y. Wu, W. Song, X. Wang, L. Guo, M. Khan, S. Wang, F. Zhou, Y. Ling, Characterization and optimization of highly active and Ba-deficient $\text{BaCo}_{0.4}\text{Fe}_{0.4}\text{Zr}_{0.1}\text{Y}_{0.1}\text{O}_{3-\delta}$ -based cathode materials for protonic ceramics fuel cells, *Ceram. Int.* 45 (2019) 18583–18591, <https://doi.org/10.1016/j.ceramint.2019.06.081>.
- [20] Z. Wang, Y. Wang, J. Wang, Y. Song, M.J. Robson, A. Seong, M. Yang, Z. Zhang, A. Belotti, J. Liu, G. Kim, J. Lim, Z. Shao, F. Ciucci, Rational design of perovskite ferrites as high-performance proton-conducting fuel cell cathodes, *Nat. Catal.* 5 (2022) 777–787, <https://doi.org/10.1038/s41929-022-00829-9>.
- [21] F. Dong, D. Chen, Y. Chen, Q. Zhao, Z. Shao, La-doped $\text{BaFeO}_{3-\delta}$ perovskite as a cobalt-free oxygen reduction electrode for solid oxide fuel cells with oxygen-ion conducting electrolyte, *J. Mater. Chem.* 22 (2012) 15071–15079, <https://doi.org/10.1039/c2jm31711g>.
- [22] G. Raimondi, R. Merkle, J. Maier, Impact of first-row transition metals in (Ba,La) (Fe,TM) $\text{O}_{3-\delta}$ on proton uptake and electronic conductivity, *Solid State Ion.* 391 (2023) 116143, <https://doi.org/10.1016/j.ssi.2023.116143>.
- [23] H. Dai, X. Xu, C. Liu, C. Ma, Q. Zhang, L. Bi, Tailoring a LaMnO_3 cathode for proton-conducting solid oxide fuel cells: integration of high performance and excellent stability, *J. Mater. Chem. A* 9 (2021) 12553–12564, <https://doi.org/10.1039/d1ta01221e>.
- [24] Y. Gu, R. Peng, P. Xiong, S. Li, Z. Wang, H. Dai, L. Bi, Electrochemical evaluation of $\text{Pr}_{1.85}\text{M}_{0.15}\text{NiO}_{4+x}$ (M=Ba, Sr, Ca) cathodes for protonic ceramic fuel cells, *Ceram. Int.* (2024), <https://doi.org/10.1016/j.ceramint.2024.03.029>.
- [25] S. Yoo, A. Jun, Y.-W. Ju, D. Odkhuu, J. Hyodo, H.Y. Jeong, N. Park, J. Shin, T. Ishihara, G. Kim, Development of double-perovskite compounds as cathode materials for low-temperature solid oxide fuel cells, *Angew. Chem. -Int. Ed.* 53 (2014) 13064–13067, <https://doi.org/10.1002/anie.201407006>.
- [26] Y. Zhou, E. Liu, Y. Chen, Y. Liu, L. Zhang, W. Zhang, Z. Luo, N. Kane, B. Zhao, L. Soule, Y. Niu, Y. Ding, H. Ding, D. Ding, M. Liu, An active and robust air electrode for reversible protonic ceramic electrochemical cells, *ACS Energy Lett.* 6 (2021) 1511–1520, <https://doi.org/10.1021/acsenenerglett.1c00432>.
- [27] A.J.E. Rowberg, L. Weston, C.G. Van de Walle, Optimizing proton conductivity in zirconates through defect engineering, *ACS Appl. Energy Mater.* 2 (2019) 2611–2619, <https://doi.org/10.1021/acsaem.8b02222>.
- [28] Z. Huang, Y. Yang, H. Lv, C. Shi, T. Li, Y. Ling, T. Chen, S. Wang, Large-area anode-supported protonic ceramic fuel cells combining with multilayer-tape casting and hot-pressing lamination technology, *J. Eur. Ceram. Soc.* 43 (2023) 428–437, <https://doi.org/10.1016/j.jeurceramsoc.2022.09.057>.
- [29] T.H. Wan, M. Saccoccio, C. Chen, F. Ciucci, Influence of the discretization methods on the distribution of relaxation times deconvolution: implementing radial basis functions with DRTtools, *Electrochim. Acta* 184 (2015) 483–499, <https://doi.org/10.1016/j.electacta.2015.09.097>.
- [30] F. Ciucci, C. Chen, Analysis of electrochemical impedance spectroscopy data using the distribution of relaxation times: a Bayesian and hierarchical Bayesian approach, *Electrochim. Acta* 167 (2015) 439–454, <https://doi.org/10.1016/j.electacta.2015.03.123>.
- [31] J. Liu, T.H. Wan, F. Ciucci, A. Bayesian, view on the Hilbert transform and the Kramers-Kronig transform of electrochemical impedance data: probabilistic estimates and quality scores, *Electrochim. Acta* 357 (2020) 136864, <https://doi.org/10.1016/j.electacta.2020.136864>.
- [32] T.D. Kuehne, M. Iannuzzi, M. Del Ben, V.V. Rybkin, P. Seewald, F. Stein, T. Laino, R.Z. Khaliullin, O. Schutt, F. Schiffrmann, D. Golze, J. Wilhelm, S. Chulkov, M. H. Bani-Hashemian, V. Weber, U. Borstnik, M. Taillefumier, A.S. Jakobovits, A. Lazzaro, H. Pabst, T. Mueller, R. Schade, M. Guidon, S. Andermatt, N. Holmberg, G.K. Schenter, A. Hehn, A. Bussy, F. Belleflamme, G. Tabacchi, A. Gloss, M. Lass, I. Bethune, C.J. Mundy, C. Plessl, M. Watkins, J. VandeVondele, M. Krack, J. Hutter, CP2K: An electronic structure and molecular dynamics software package - quickstep: efficient and accurate electronic structure calculations, *J. Chem. Phys.* 152 (2020), <https://doi.org/10.1063/5.0007045>.
- [33] D. Liu, Y. Dou, T. Xia, Q. Li, L. Sun, L. Huo, H. Zhao, B-site La, Ce, and Pr-doped $\text{Ba}_{0.5}\text{Sr}_{0.5}\text{Co}_{0.7}\text{Fe}_{0.3}\text{O}_{3-\delta}$ perovskite cathodes for intermediate-temperature solid oxide fuel cells: Effectively promoted oxygen reduction activity and operating stability, *J. Power Sources* 494 (2021) 229778, <https://doi.org/10.1016/j.jpowsour.2021.229778>.
- [34] M. Li, Y. Wang, Y. Wang, F. Chen, C. Xia, Bismuth doped lanthanum ferrite perovskites as novel cathodes for intermediate-temperature solid oxide fuel cells, *ACS Appl. Mater. Interfaces* 6 (2014) 11286–11294, <https://doi.org/10.1021/am5017045>.
- [35] Z. Liu, D. Cheng, Y. Zhu, M. Liang, M. Yang, G. Yang, R. Ran, W. Wang, W. Zhou, Z. Shao, Robust bifunctional phosphorus-doped perovskite oxygen electrode for reversible proton ceramic electrochemical cells, *Chem. Eng. J.* 450 (2022) 137787, <https://doi.org/10.1016/j.cej.2022.137787>.
- [36] T. Hong, W. Lu, K. Ren, T. Liu, The two-fold diffusion process for proton uptake reaction in $\text{BCFZY } e^-/\text{H}^+/\text{O}^{2-}$ triple conductor measured by electrical conductivity relaxation, *IONICS* 26 (2020) 5293–5297, <https://doi.org/10.1007/s11581-020-03757-5>.
- [37] E. Kim, H.-I. Yoo, Two-fold-to-single-fold transition of the conductivity relaxation patterns of proton-conducting oxides upon hydration/dehydration, *Solid State Ion.* 252 (2013) 132–139, <https://doi.org/10.1016/j.ssi.2013.04.005>.
- [38] P. Zhong, K. Toyoura, L. Jiang, L. Chen, S.A. Ismail, N. Hatada, T. Norby, D. Han, Protonic conduction in $\text{La}_2\text{NiO}_{4+\delta}$ and $\text{La}_{2-x}\text{A}_x\text{NiO}_{4+\delta}$ (A = Ca, Sr, Ba) Ruddlesden-popper type oxides, advanced energy, *Adv. Energy Mater.* 12 (2022) 2200392, <https://doi.org/10.1002/aenm.202200392>.
- [39] L. Chen, G. Wang, K. Toyoura, D. Han, High-temperature protonic conduction in $\text{La}_2\text{NiO}_{4+\delta}$ -based Ruddlesden-popper type oxides: correlation with concentration of interstitial oxide ions (n/a), *Small* (2024) 2311473, <https://doi.org/10.1002/sml.202311473>.
- [40] N.A. Merino, B.P. Barbero, P. Eloy, L.E. Cadús, $\text{La}_{1-x}\text{Ca}_x\text{CoO}_3$ perovskite-type oxides: identification of the surface oxygen species by XPS, *Appl. Surf. Sci.* 253 (2006) 1489–1493, <https://doi.org/10.1016/j.apsusc.2006.02.035>.
- [41] Z. Liu, Y. Lin, H. Nie, D. Liu, Y. Li, X. Zhao, T. Li, G. Yang, Y. Sun, Y. Zhu, W. Wang, R. Ran, W. Zhou, Z. Shao, Highly active nanocomposite air electrode with fast proton diffusion channels via Er doping-induced phase separation for reversible proton ceramic electrochemical cells, *Adv. Funct. Mater.* 34 (2024) 2311140, <https://doi.org/10.1002/adfm.202311140>.
- [42] B. Qian, C. Liu, S. Wang, B. Yin, Y. Zheng, L. Ge, H. Chen, C. Zhang, Ca-doped $\text{La}_{0.75}\text{Sr}_{0.25}\text{Cr}_{0.5}\text{Mn}_{0.5}\text{O}_3$ cathode with enhanced CO_2 electrocatalytic performance for high-temperature solid oxide electrolysis cells, *Int. J. Hydrog. Energy* 46 (2021) 33349–33359, <https://doi.org/10.1016/j.ijhydene.2021.07.174>.
- [43] X. Kuai, G. Yang, Y. Chen, H. Sun, J. Dai, Y. Song, R. Ran, W. Wang, W. Zhou, Z. Shao, Boosting the activity of $\text{BaCo}_{0.4}\text{Fe}_{0.4}\text{Zr}_{0.1}\text{Y}_{0.1}\text{O}_{3-\delta}$ perovskite for oxygen reduction reactions at low-to-intermediate temperatures through tuning B-site cation deficiency, *Adv. Energy Mater.* 9 (2019) 1902384, <https://doi.org/10.1002/aenm.201902384>.
- [44] R. Zhang, A. Villanueva, H. Alamdari, S. Kaliaguine, Catalytic reduction of NO by propene over $\text{LaCo}_{1-x}\text{Cu}_x\text{O}_3$ perovskites synthesized by reactive grinding, *Appl. Catal. B: Environ.* 64 (2006) 220–233, <https://doi.org/10.1016/j.apcatb.2005.10.028>.
- [45] W. Tang, H. Ding, W. Bian, C.Y.R. Vera, J.Y. Gomez, Y. Dong, J. Li, W. Wu, W. Fan, M. Zhou, C. Gore, B.M. Blackburn, H. Luo, D. Ding, An unbalanced battle in excellence: revealing effect of ni/co occupancy on water splitting and oxygen

- reduction reactions in triple-conducting oxides for protonic ceramic electrochemical cells, *Small* 18 (2022), <https://doi.org/10.1002/smll.202201953>.
- [46] X. Zhang, R. Song, D. Huan, K. Zhu, X. Li, H. Han, C. Xia, R. Peng, Y. Lu, Surface self-assembly protonation triggering triple-conductive heterostructure with highly enhanced oxygen reduction for protonic ceramic fuel cells, *Small* 18 (2022), <https://doi.org/10.1002/smll.202205190>.
- [47] Z. Luo, Y. Zhou, X. Hu, W. Wang, Y. Ding, W. Zhang, T. Li, N. Kane, Z. Liu, M. Liu, A new class of proton conductors with dramatically enhanced stability and high conductivity for reversible solid oxide cells, *Small* 19 (2023), <https://doi.org/10.1002/smll.202208064>.
- [48] X. Li, X. Jiang, H. Xu, Q. Xu, L. Jiang, Y. Shi, Q. Zhang, Scandium-doped $\text{PrBaCo}_{2-x}\text{Sc}_x\text{O}_{6-\delta}$ oxides as cathode material for intermediate-temperature solid oxide fuel cells, *Int. J. Hydrog. Energy* 38 (2013) 12035–12042, <https://doi.org/10.1016/j.ijhydene.2013.07.024>.
- [49] M.S.I. Sozal, W. Tang, S. Das, W. Li, A. Durygin, V. Drozd, C. Zhang, B. Jafarizadeh, C. Wang, A. Agarwal, D. Ding, Z. Cheng, Electrical, thermal, and H_2O and CO_2 poisoning behaviors of $\text{PrNi}_{0.5}\text{Co}_{0.5}\text{O}_{3-\delta}$ electrode for intermediate temperature protonic ceramic electrochemical cells, *Int. J. Hydrog. Energy* 47 (2022) 21817–21827, <https://doi.org/10.1016/j.ijhydene.2022.05.011>.
- [50] Y.G. Lyagaeva, D.A. Medvedev, A.K. Demin, P. Tsiakaras, O.G. Reznitskikh, Thermal expansion of materials in the barium cerate-zirconate system, *Phys. Solid State* 57 (2015) 285–289, <https://doi.org/10.1134/S1063783415020250>.
- [51] Z. Zhu, J. Qian, Z. Wang, J. Dang, W. Liu, High-performance anode-supported solid oxide fuel cells based on nickel-based cathode and $\text{Ba}(\text{Zr}_{0.1}\text{Ce}_{0.7}\text{Y}_{0.2})\text{O}_{3-\delta}$ electrolyte, *J. Alloy. Compd.* 581 (2013) 832–835, <https://doi.org/10.1016/j.jallcom.2013.07.210>.
- [52] M. Ghamarinia, A. Babaei, C. Zamani, H. Aslannejad, Application of the distribution of relaxation time method in electrochemical analysis of the air electrodes in the SOFC/SOEC devices: a review, *Chem. Eng. J. Adv.* 15 (2023) 100503, <https://doi.org/10.1016/j.cej.2023.100503>.
- [53] D.A. Osinkin, An approach to the analysis of the impedance spectra of solid oxide fuel cell using the DRT technique, *Electrochim. Acta* 372 (2021) 137858, <https://doi.org/10.1016/j.electacta.2021.137858>.
- [54] Z. Liu, Z. Tang, Y. Song, G. Yang, W. Qian, M. Yang, Y. Zhu, R. Ran, W. Wang, W. Zhou, Z. Shao, High-entropy perovskite oxide: a new opportunity for developing highly active and durable air electrode for reversible protonic ceramic electrochemical cells, *Nano-Micro Lett.* 14 (2022), <https://doi.org/10.1007/s40820-022-00967-6>.
- [55] W. Wang, D. Medvedev, Z. Shao, Gas humidification impact on the properties and performance of perovskite-type functional materials in proton-conducting solid oxide cells, *Adv. Funct. Mater.* 28 (2018) 1802592, <https://doi.org/10.1002/adfm.201802592>.
- [56] Z. Wang, P. Lv, L. Yang, R. Guan, J. Jiang, F. Jin, T. He, $\text{Ba}_{0.95}\text{La}_{0.05}\text{Fe}_{0.8}\text{Zn}_{0.2}\text{O}_{3-\delta}$ cobalt-free perovskite as a triple-conducting cathode for proton-conducting solid oxide fuel cells, *Ceram. Int.* 46 (2020) 18216–18223, <https://doi.org/10.1016/j.ceramint.2020.04.144>.
- [57] Y. Song, J. Liu, Y. Wang, D. Guan, A. Seong, M. Liang, M.J. Robson, X. Xiong, Z. Zhang, G. Kim, Z. Shao, F. Ciucci, Nanocomposites: a new opportunity for developing highly active and durable bifunctional air electrodes for reversible protonic ceramic cells, *Adv. Energy Mater.* 11 (2021) 2101899, <https://doi.org/10.1002/aenm.202101899>.
- [58] R. Ren, Z. Wang, X. Meng, X. Wang, C. Xu, J. Qiao, W. Sun, K. Sun, Tailoring the oxygen vacancy to achieve fast intrinsic proton transport in a perovskite cathode for protonic ceramic fuel cells, *ACS Appl. Energy Mater.* 3 (2020) 4914–4922, <https://doi.org/10.1021/acsaem.0c00486>.
- [59] H. Shi, Y. Hu, Z. Feng, J. Qu, Y. Yu, D. Zhang, W. Tan, Solid-state synthesis of $\text{BaCe}_{0.16}\text{Y}_{0.04}\text{Fe}_{0.8}\text{O}_{3-\delta}$ cathode for protonic ceramic fuel cells, *Asia-Pac. J. Chem. Eng.* 17 (2022), <https://doi.org/10.1002/apj.2789>.
- [60] G. Xue, J. Li, H. Wang, H. Sun, X. Guo, Q. Hu, $(\text{Pr}_{0.9}\text{La}_{0.1})_{1.9}(\text{Ni}_{0.7}\text{Cu}_{0.3})_{0.9}\text{Mn}_{0.1}\text{O}_{4+\delta}$ nanofiber cathode with Pr site cation defect prepared by electrospinning and its application in reversible fuel cells, *J. Power Sources* 552 (2022) 232220, <https://doi.org/10.1016/j.jpowsour.2022.232220>.
- [61] T. Hu, F. Zhu, J. Xia, F. He, Z. Du, Y. Zhou, Y. Liu, H. Wang, Y. Chen, In situ engineering of a cobalt-free perovskite air electrode enabling efficient reversible oxygen reduction/evolution reactions, *Adv. Funct. Mater.* 33 (2023), <https://doi.org/10.1002/adfm.202305567>.
- [62] N. Tsvetkov, Q. Lu, L. Sun, E.J. Crumlin, B. Yildiz, Improved chemical and electrochemical stability of perovskite oxides with less reducible cations at the surface, *Nat. Mater.* 15 (2016) 1010–1016, <https://doi.org/10.1038/NMAT4659>.
- [63] Y. Chen, Y. Chen, D. Ding, Y. Ding, Y. Choi, L. Zhang, S. Yoo, D. Chen, B. Deglee, H. Xu, Q. Lu, B. Zhao, G. Vardar, J. Wang, H. Bluhm, E.J. Crumlin, C. Yang, J. Liu, B. Yildiz, M. Liu, A robust and active hybrid catalyst for facile oxygen reduction in solid oxide fuel cells, *Energy Environ. Sci.* 10 (2017) 964–971, <https://doi.org/10.1039/c6ee03656b>.
- [64] R. Jacobs, J. Hwang, Y. Shao-Horn, D. Morgan, Assessing correlations of perovskite catalytic performance with electronic structure descriptors, *Chem. Mater.* 31 (2019) 785–797, <https://doi.org/10.1021/acs.chemmater.8b03840>.
- [65] J. Li, N. Sun, X. Liu, Y. Shen, F. Wang, J. Li, K. Shi, F. Jin, Investigation on $\text{Nd}_{1-x}\text{Ca}_x\text{BaCo}_2\text{O}_{5+\delta}$ double perovskite as new oxygen electrode materials for reversible solid oxide cells, *J. Alloy. Compd.* 913 (2022) 165245, <https://doi.org/10.1016/j.jallcom.2022.165245>.
- [66] K. Zhu, Y. Yang, D. Huan, X. Hu, N. Shi, Y. Xie, X. Li, C. Xia, R. Peng, Y. Lu, Theoretical and experimental investigations on K-doped $\text{SrCo}_{0.9}\text{Nb}_{0.1}\text{O}_{3-\delta}$ as a promising cathode for proton-conducting solid oxide fuel cells, *Chemsuschem* 14 (2021) 3876–3886, <https://doi.org/10.1002/cssc.202101100>.
- [67] Z. Tao, G. Hou, N. Xu, X. Chen, Q. Zhang, Pr doped barium cerate as the cathode material for proton-conducting SOFCs, *Fuel Cells* 14 (2014) 135–138, <https://doi.org/10.1002/fuce.201300205>.
- [68] Y. Chen, S. Yoo, K. Pei, D. Chen, L. Zhang, B. deGlee, R. Murphy, B. Zhao, Y. Zhang, Y. Chen, M. Liu, An in situ formed, dual-phase cathode with a highly active catalyst coating for protonic ceramic fuel cells, *Adv. Funct. Mater.* 28 (2018) 1704907, <https://doi.org/10.1002/adfm.201704907>.
- [69] H. Tang, Z. Jin, Y. Wu, W. Liu, L. Bi, Cobalt-free nanofiber cathodes for proton conducting solid oxide fuel cells, *Electrochem. Commun.* 100 (2019) 108–112, <https://doi.org/10.1016/j.elecom.2019.01.022>.
- [70] Q. Wang, J. Hou, Y. Fan, X.-a. Xi, J. Li, Y. Lu, G. Huo, L. Shao, X.-Z. Fu, J.-L. Luo, $\text{Pr}_2\text{BaNiMnO}_{7.8}$ double-layered Ruddlesden-Popper perovskite oxides as efficient cathode electrocatalysts for low temperature proton conducting solid oxide fuel cells, *J. Mater. Chem. A* 8 (2020) 7704–7712, <https://doi.org/10.1039/c9ta11212j>.
- [71] G. Li, Y. Gou, R. Ren, C. Xu, J. Qiao, W. Sun, Z. Wang, K. Sun, Fluorinated $\text{Pr}_2\text{NiO}_{4+\delta}$ as high-performance air electrode for tubular reversible protonic ceramic cells, *J. Power Sources* 508 (2021) 230343, <https://doi.org/10.1016/j.jpowsour.2021.230343>.
- [72] H. Tong, M. Fu, Y. Yang, F. Chen, Z. Tao, A novel self-assembled cobalt-free perovskite composite cathode with triple-conduction for intermediate proton-conducting solid oxide fuel cells, *Adv. Funct. Mater.* 32 (2022) 2209695, <https://doi.org/10.1002/adfm.202209695>.
- [73] F. Zhu, F. He, D. Liu, H. Zhang, Y. Xu, K. Xu, Y. Chen, A surface reconfiguration of a perovskite air electrode enables an active and durable reversible protonic ceramic electrochemical cell, *Energy Storage Mater.* 53 (2022) 754–762, <https://doi.org/10.1016/j.ensm.2022.10.009>.
- [74] T. Hu, Y. Xu, K. Xu, F. Zhu, Y. Chen, Visiting the roles of Sr- or Ca- doping on the oxygen reduction reaction activity and stability of a perovskite cathode for proton conducting solid oxide fuel cells, *Susmat* 3 (2023) 91–101, <https://doi.org/10.1002/sus2.101>.